Coupling between magnetic and thermodynamic properties in $R\mathrm{Rh_2Si_2}$ ($R = $ Dy, Ho)

H. Dawczak-Dębicki,[1] K. Kliemt [ORCID],[2] M. V. Ale Crivillero [ORCID],[1] R. Küchler,[1] C. Krellner,[2] O. Stockert,[1] and S. Wirth [ORCID][1,*]

[1]*Max Planck Institute for Chemical Physics of Solids, D-01187 Dresden, Germany*
[2]*Kristall- und Materiallabor, Physikalisches Institut, Goethe-Universität Frankfurt, D-60438 Frankfurt/M, Germany*

Single crystals of $\mathrm{DyRh_2Si_2}$ and $\mathrm{HoRh_2Si_2}$ were investigated by thermal expansion and magnetostriction. The different types of magnetic order can clearly be seen in these measurements, particularly the canting of the moments away from the crystallographic c direction below about 12 K and the spin flip for magnetic field applied along the c direction. For $\mathrm{HoRh_2Si_2}$, an additional transition just below T_N is analyzed by means of the Grüneisen ratio and is likely caused by a change in the magnetic structure. Our results nicely corroborate findings from other magnetic and thermodynamic measurements on these materials and provide further evidence suggesting the formation of magnetic domains.

I. INTRODUCTION

Materials crystallizing in the $\mathrm{ThCr_2Si_2}$-type structure (space group $I4/mmm$) exhibit a variety of interesting physical phenomena [1], including superconductivity [2–4]. More specifically, the discovery of superconductivity in some rare-earth compounds of this family [5–9] provided enormous insight into, and propelled, the field of heavy-fermion physics and beyond [8,10,11]. In particular, these compounds gave some valuable insight concerning the pivotal impact of magnetism on unconventional superconductivity and quantum criticality [12]. In consequence, it is vital to deepen our understanding of the variety of magnetic properties and phenomena of these materials [13].

Even within the rare-earth 122 series the magnetic properties vary widely. Ce- and Yb-based materials often exhibit noninteger valencies of the rare-earth (R) element and are discussed in terms of Ruderman-Kittel-Kasuya-Yosida (RKKY) interaction [14–16] mediated via a polarization of the conduction electrons. This interaction can compete with the Kondo effect, an on-site screening of the $4f$ moments by the conduction electrons [3]. For stable, trivalent R elements like Nd, Gd, Tb, Ho, and Er, the RKKY interaction results in local moment antiferromagnetic (AFM) order, often with a simple propagation vector of $\mathbf{Q} = (001)$ and ferromagnetic ordering within the plane perpendicular to (001) [17–24]. In many compounds the local moments align along the crystallographic c direction, while for $\mathrm{SmRh_2Si_2}$, $\mathrm{GdRh_2Si_2}$, and $\mathrm{GdIr_2Si_2}$ an orientation in the ab plane is reported [23–25],

which, in the case of $\mathrm{GdRh_2Si_2}$, can even be temperature dependent [26]. Here, it should be noted that in R-based compounds the spin-orbit coupling is generally larger than the crystal field effects [27]. In addition, anisotropic exchange was discussed for $\mathrm{TbRh_2Si_2}$ [28]. It should also be noted that d electrons of the transition elements (e.g., Rh, Ru) contribute very little to the total magnetic moment; the value of $\sim 0.002\mu_B$ for Rh in $\mathrm{DyRh_2Si_2}$ is too small to be detected in neutron diffraction [17,19]. In the case of $R = $ Gd, there can also be a small contribution from Gd $5d$ electrons, $\sim 0.28\mu_B$ in $\mathrm{GdRh_2Si_2}$ [29].

Exceptions to the above-mentioned magnetic configuration are $\mathrm{DyRh_2Si_2}$ and $\mathrm{HoRh_2Si_2}$, in which the magnetic moments were found to be canted away from the crystallographic c axis by neutron diffraction [17,19]. For both compounds, the magnetic properties and specific heat measurements were analyzed in terms of a mean-field model [30–33]. Yet based on magnetic susceptibility and specific heat measurements, a so-called component-separated magnetic transition, stemming from multiple interactions, was suggested for $\mathrm{HoRh_2Si_2}$ [34], in analogy to the tetragonal compound $\mathrm{TbCoGa_5}$ [35]. To gain further insight, measurements of thermodynamic properties are called for, in particular those that provide information along different crystallographic directions of the sample. Therefore, we conducted measurements of thermal expansion and magnetostriction on single-crystalline $\mathrm{DyRh_2Si_2}$ and $\mathrm{HoRh_2Si_2}$. To allow for comparison to data from the literature, magnetic susceptibility was also measured on the same samples.

II. EXPERIMENT

The single crystals of $\mathrm{DyRh_2Si_2}$ and $\mathrm{HoRh_2Si_2}$ used in this study were grown from In flux employing a modified Bridgman technique; details of the growth procedure were provided in Ref. [36]. X-ray diffraction on powdered single crystals was conducted (using copper $K\alpha$ radiation in a Bruker D8 diffractometer) to confirm the crystallographic structure

---

*steffen.wirth@cpfs.mpg.de

and quality of the samples. The crystallographic orientation of the single crystals was determined by Laue diffraction. The samples typically grew in a plateletlike shape with the crystallographic c direction (the long axis of the tetragonal unit cell) along the thin sample dimension. In most cases, the other sample edges were parallel to the $\langle 110 \rangle$ crystallographic directions.

The thermal expansion and magnetostriction measurements were performed using a dilatometer cell as described in Refs. [37,38]. Our cell is equipped with a calibrated Cernox thermometer close to the sample [37], and hence, the accuracy of all respective temperatures is better than 0.1 K. The measurements were conducted in a physical property measurement system (PPMS) by Quantum Design with a maximum magnetic field of 9 T applied parallel to the sample dilatation direction investigated. Here, special attention was paid to minimizing electrical noise [38]. Whenever possible, identical samples were used for measurements along different crystallographic directions. However, in some cases samples were chosen according to their specific shape in order to optimize the dilatometer signal for the crystallographic direction to be measured and to assist sample mounting. Typical sample dimensions were 1–2 mm in the ab plane and up to 0.6 mm along the c direction. Data for the thermal expansion were taken upon warming the sample (if not stated otherwise) and repeated at least once for comparison. Between cycles of magnetostriction measurements (i.e., measurements at constant temperature) the sample was warmed up to at least 80 K, i.e., into the paramagnetic state well above the Néel temperatures $T_N \approx 55$ K for DyRh$_2$Si$_2$ and $T_N \approx 29$ K for HoRh$_2$Si$_2$. We note that different samples gave somewhat different results for the thermal expansion and magnetostriction, particularly in the temperature range around T_1 and for small magnetic fields, respectively, as discussed below. The observed temperatures and magnetic fields of the transitions, however, reproduced very well.

Measurements of the magnetic dc susceptibilities were conducted in a magnetic property measurement system (MPMS3 by Quantum Design) using the same samples as for the thermal expansion and magnetostriction measurements. For these measurements, a magnetic field of 25 Oe (corrected for the remnant field of the superconducting magnet as determined by a Pd reference) was applied. The temperature accuracy is given by the lower of $\pm 1\%$ or ± 0.5 K [39]. The PPMS, equipped with a calorimeter that utilizes a quasia-diabatic thermal relaxation technique, was also used for measurements of the heat capacitance. For the investigation of possible first-order transitions, we used a single-slope analysis of the measured heat pulses, as described in Ref. [40].

III. RESULTS

A. HoRh$_2$Si$_2$

The results of dc susceptibility χ measurements for HoRh$_2$Si$_2$ along different crystallographic directions are presented in Fig. 1(a). The Néel temperature of $T_N = 29.0 \pm 0.3$ K is clearly observed when measured along the (001) direction. Additional small humps can be recognized upon zoom into the low-temperature data [red data in Fig. 1(b)] at
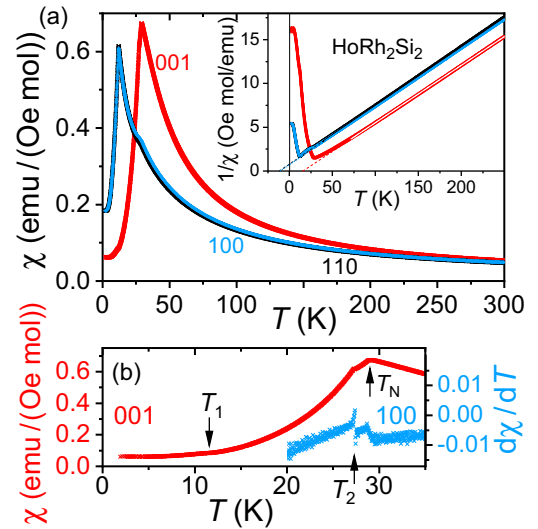
FIG. 1. (a) dc susceptibility χ measured for HoRh$_2$Si$_2$ along three different crystallographic directions in a field of 25 Oe. Data for (100) (blue) and (110) (black) are very similar. The inset shows the inverse of the susceptibilities. The dashed lines represent extrapolations of the linear fits to $1/\chi$. (b) Zoom of the low-T data of $\chi(T)$ for the (001) direction (red). The right scale visualizes $d\chi(T)/dT$ (blue, in units of emu Oe^{-1} mol^{-1} K^{-1}) within $20 \leqslant T \leqslant 35$ K along the (100) direction. Arrows mark the small hump at $T_1 = 11.7$ K and features at $T_2 = 27.3$ K and $T_N = 29.0$ K. Note the uniform color code for the different directions in all plots.

$T_2 = 27.3 \pm 0.3$ K and $T_1 = 11.7 \pm 0.2$ K [the latter can also be seen in the $1/\chi$ plot; inset of Fig. 1(a)]. Along the (100) and (110) directions, $\chi(T)$ peaks sharply at 11.9 K, i.e., at the temperature of the small hump in $\chi(T)$ along (001), while small kinks are seen at T_N. Only upon taking the derivatives $d\chi(T)/dT$ do these small kinks separate into two features at ~ 27.3 and ~ 29.0 K, as shown for the (100) direction in Fig. 1(b) (blue data and right scale). All $\chi(T)$ data nicely follow a Curie-Weiss law in the paramagnetic regime, as is obvious from plots of $1/\chi$ in the inset of Fig. 1(a) [41]. The fits yield effective moments of $\mu_{\text{eff}} \approx (10.9 \pm 0.2)\mu_B$, which is slightly larger than the expected value of $10.61 \mu_B$ for Ho^{3+} (where μ_B is the Bohr magneton). This may be attributed to the small magnetic field applied during the susceptibility measurements and the resulting impact of the remnant field. The obtained Weiss temperatures are $\theta_c \sim 16 \pm 0.4$ K along the c direction, indicative of dominating ferromagnetic interactions, and $\theta_{ab} \sim -11 \pm 0.3$ K within the ab plane (dominating antiferromagnetic interactions). All results are in good agreement with reported ones [17,34,36,42–45] and confirm the magnetic properties as outlined in the Introduction. The observation of two transitions near T_N along all measured directions indicates high sample quality and is likely related to changes in the magnetic structure (see Sec. IV).

The magnetic field H dependence of magnetization M measured at $T = 2$ K and with H applied along different crystallographic directions is presented in Fig. 2. Even for $\vec{H} \parallel (001)$, the expected saturation magnetic moment of Ho^{3+}, $g\mu_B J = 10 \mu_B$, is not observed for $\mu_0 H \leqslant 9$ T. However, the two-step magnetization increase of about $4\mu_B$ per step
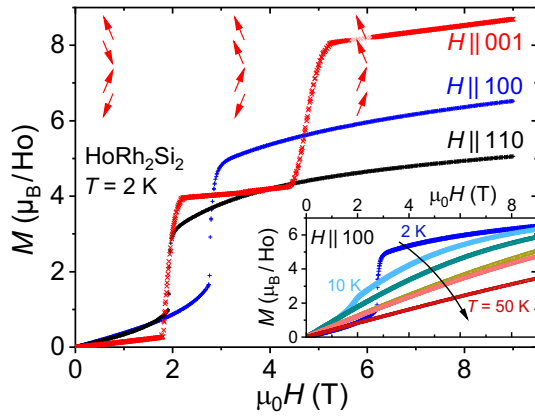
FIG. 2. Field dependence of magnetization M measured at 2 K and for magnetic fields H applied along different directions (as indicated). The red arrows sketch the evolution of the Ho moment arrangement for $\vec{H} \parallel (001)$ along the c direction and for two magnetic domains. The inset shows the temperature evolution of $M(H)$ for $\vec{H} \parallel (100)$ at $T = 2, 10, 15, 26, 28$, and 50 K.

FIG. 3. Magnetostriction $\Delta L(H)/L_0$ of HoRh$_2$Si$_2$ measured at $T = 1.8$ K with magnetic fields applied along the (100) crystallographic direction while sweeping the field up (red) and down (blue). Inset: Magnetostriction coefficient $\lambda = (1/L_0)\,\partial L/\partial H$.

agrees well with the reported canting of the magnetic moments away from the crystallographic c direction by $\sim 28°$ at $T = 4.2$ K [17]. The two-step magnetization increase itself is a consequence of the propagation vector $\vec{k} = (0, 0, 1)$ and a change in magnetic configuration with increasing H from an AFM $+ - + -$ state at $\mu_0 H \lesssim 1.8$ T to $+ + + -$ and, finally, a tilted, field-polarized $+ + + +$ state beyond 5 T [17,44].

The tetragonal ThCr$_2$Si$_2$ structure can give rise to the formation of magnetic domains [46,47]. In addition, the canting of the magnetic moments away from the c direction allows for so-called orientation domains within which the ab component of the magnetization is oriented differently [47]. For $\vec{H} \parallel (100)$, this basal plane component of the moments within the differently oriented magnetic domains is initially rotated toward the field direction and then flips to the (100) direction parallel to $\vec{H}$ near 2.8 T. This is suggested by the magnetization value of approximately $4.9\mu_B$ at fields just beyond the flip which is only slightly larger than the expected value for a canting angle of 28°. At $T = 10$ K, this canting angle is markedly smaller, and hence, a considerably smaller magnetization value is observed beyond the flip (see the inset of Fig. 2). For $T > T_1$, i.e., without canting, such a flip of the magnetization is neither expected nor observed. The magnetization behavior for $\vec{H} \parallel (110)$ is qualitatively very similar to the observations for $\vec{H} \parallel (100)$; the smaller magnetization values for large fields, however, indicate the (110) direction is magnetically harder than the (100) direction. We note that our $M(H)$ curve for (001) is very similar to the one reported in [44], although there are quantitative differences for (110) and a qualitatively different behavior for (100).

Large magnetostriction is commonly observed in rare-earth-containing compounds due to their orbital magnetism. Within a quadrupole approximation, the $4f$ electron densities of Ho^{3+} and Dy^{3+} retain an oblate shape [27]. In Fig. 3, the magnetostriction $\Delta L(H)/L_0$ [where $L_0(T) = L(T, H = 0)$] and its coefficient $\lambda = (1/L_0)\,\partial L/\partial H$ at $T = 1.8$ K are presented for $\vec{H} \parallel (100)$. These data are in excellent agreement with the $M(H)$ data in Fig. 2. We observe a large increase of
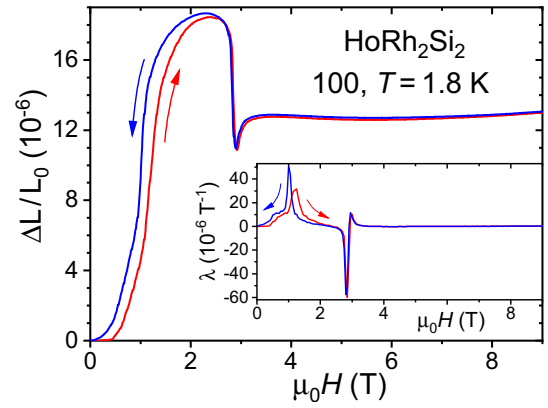
$L(H)$ upon rotation of the in-plane component of magnetization, while the flip at $\mu_0 H \approx 2.8$ T results in a sudden drop in $L(H)$. As expected from this scenario, the length change for fields above 3 T is very small. The discrepancy between the magnetostriction measured during up sweep (red lines in Fig. 3) and down sweep (blue) is in line with a scenario involving different magnetic domains in this tetragonal material.

Figure 4 exhibits the relative length changes $\Delta L_i(T)/L_i$ and the uniaxial thermal expansion coefficients $\alpha_i = (1/L_i)(dL_i/dT)$ for HoRh$_2$Si$_2$. Here, the index i denotes
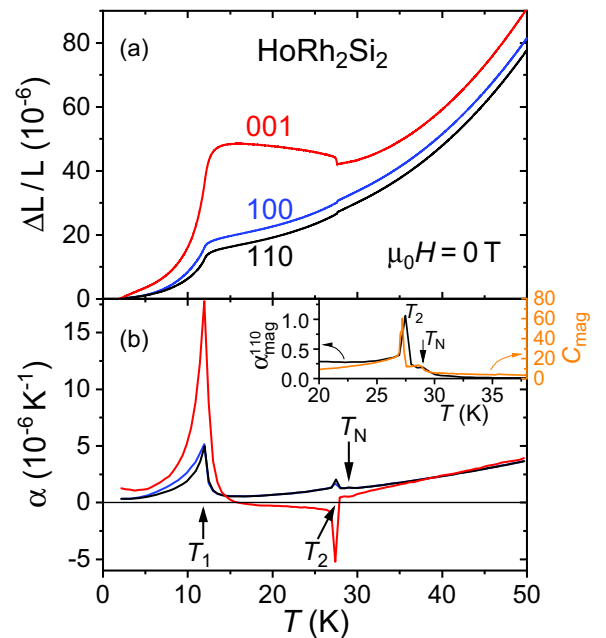
FIG. 4. (a) Relative length change $\Delta L(T)/L$ and (b) thermal expansion coefficient $\alpha(T)$ of HoRh$_2$Si$_2$ measured along different crystallographic directions in the temperature range $2 \leqslant T \leqslant 50$ K. Inset: Comparison between α_{mag}^{110}, the magnetic contribution to α_{110} along the (110) direction, and C_{mag} from Fig. 5(a). α_{mag}^{110} (black, left scale) is given in units of 10^{-6} K^{-1}, and C_{mag} (orange, right scale) is in J mol^{-1} K^{-1}.

measurements along the different crystallographic directions (100), (110), and (001). Clearly, strong maxima in $\alpha_i(T)$ are observed at $T_1 = 11.8$ K for all directions, a temperature which agrees well with the feature observed in $\chi(T)$. Additional peaks are observed for all directions upon approaching T_N. Importantly, equal-area constructions for $\Delta L_i(T)/L_i$ yield temperatures of the jumps of 27.6 K for the (100) and (110) directions and 27.5 K for (001), i.e., very close to T_2. In contrast, only tiny variations of $\alpha(T)$ are present at T_N [see the respective arrow in Fig. 4(b)]. We note that magnetization measurements along (001) showed only a small cusp at $T_2 = 27.3$ K [44], while the magnetic specific heat peaked dramatically at this temperature (see discussion below and [34]), the latter very similar to our thermal expansion results. Clearly, our thermal expansion measurements are less sensitive to the onset of magnetic order at T_N and point to a mechanism operating at T_2 which is different from the antiferromagnetic ordering at T_N. Moreover, at T_2 the $\Delta L_i(T)/L_i$ jump occurs in opposite directions: $\Delta L_{100}(T)/L_{100}$ and $\Delta L_{110}(T)/L_{110}$ expand by about 0.45×10^{-6} (obtained from equal-area constructions around the jumps), but HoRh$_2$Si$_2$ contracts along c by $\Delta L_{001}(T)/L_{001} \approx -2.1 \times 10^{-6}$, and hence, the volume shrinks upon warming the sample through T_2. This anisotropic thermal expansion is in line with the reported increase of the c/a ratio upon cooling from room temperature to 4.2 K [17]. There is, however, no indication for any discontinuous change in the lattice constants as, e.g., observed for some ThCr$_2$Si$_2$-type phosphides [48].

We note that our repeated measurements of thermal expansion (also on different samples) all agree qualitatively but vary quantitatively for the (001) direction, particularly within the range $T_1 \lesssim T < T_2$. We speculate that domain formation may play a role in generating such quantitative differences. This is supported by the fact that the transition temperatures T_1 and T_2 themselves agree nicely for all measurements conducted.

Given this unusual behavior of the thermal expansion, we performed measurements of the specific heat $C_p(T)$ on HoRh$_2$Si$_2$. Figure 5(a) presents the $C_p(T)$ data up to $T = 70$ K, although measurements were conducted within $3 \leqslant T \leqslant 200$ K. As the main result and in support of our thermal expansion measurements, the largest peaks in $C_p(T)$ of HoRh$_2$Si$_2$ are observed at $T = 11.6$ K $\approx T_1$ and $T = 27.2$ K $\approx T_2$, while only a much less pronounced shoulder is seen at T_N [50]. At the lowest T, a Sommerfeld coefficient of $\gamma \approx 10.5 \pm 4$ mJ mol^{-1} K^{-2} is estimated from Fig. 5(b), a value close to the one (9.6 mJ mol^{-1} K^{-2}) obtained for trivalent Eu in isostructural EuCo$_2$Si$_2$ [51]. A temperature dependence of $C_p \propto T^3$ is consistent with spin-wave excitations in an antiferromagnet [52]. Nuclear contributions of Ho (with nuclear spin $I = 7/2$) to $C_p(T)$ are expected to be negligibly small at the temperatures of interest here [53,54], while phonon contributions add only minimally to the T^3 dependence of C_p. In order to evaluate the magnetic contribution C_{mag} to the total specific heat of HoRh$_2$Si$_2$, the isostructural compound LuRh$_2$Si$_2$ was taken as a nonmagnetic reference [49]. However, the mass per formula unit of LuRh$_2$Si$_2$ exceeds that of HoRh$_2$Si$_2$ by approximately 2.4%. Hence, for a more accurate estimate of the phonon contribution in HoRh$_2$Si$_2$, $C_p(T)$ of LuRh$_2$Si$_2$ was rescaled to account for its heavier atomic mass, as outlined in [54,55].
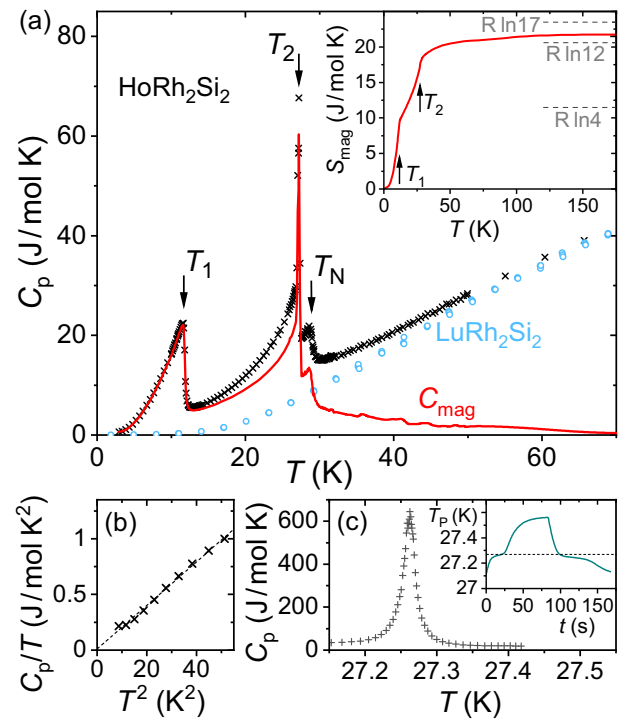
FIG. 5. (a) Temperature dependence of the specific heat $C_p(T)$ of HoRh$_2$Si$_2$ and the nonmagnetic reference compound LuRh$_2$Si$_2$ [49]. The magnetic contribution C_{mag} (red line) to $C_p(T)$ of HoRh$_2$Si$_2$ is obtained as described in the text. Inset: Magnetic entropy S_{mag} as calculated from C_{mag}. (b) $C_p(T)/T$ vs T^2 at the lowest temperatures along with a linear fit. (c) High-resolution $C_p(T)$ measurement near T_2 (see text). Inset: Arrest of the measurement platform temperature T_P at the sample's first-order transition at T_2.

The so-determined C_{mag} of HoRh$_2$Si$_2$ is shown by the red line in Fig. 5(a), and an estimate of the resulting magnetic entropy $S_{mag}(T) = \int_0^T [C_{mag}(T')/T']dT'$ is presented in the inset. Note that even at the highest $T \gg T_N$ the magnetic entropy reaches only about 88% of the expected value of $R \ln 17$ for Ho^{3+}, an observation which complicates an assessment of the associated multiplet states. Nonetheless, one may speculate from $S_{mag}(T_1) \lesssim R \ln 4$ that two doublets or one doublet and two singlets are involved below T_1. In fact, if we use the crystalline electric field (CEF) parameters as provided in [45], we find a quasiquartet ground state made up of one doublet and two singlets within an energy range of less than 0.5 K. We note that Ho^{3+} is a non-Kramers ion with four doublets and nine singlets in tetragonal symmetry [56]; a nonmagnetic singlet ground state is not evident. From the nice T^3 dependence of $C_p(T)$ gapless antiferromagnetic spin waves are expected; hence, the proposed quasiquartet ground state can be rationalized. Further, few of the singlets may reside high up in energy, which may explain the fact that the observed magnetization at 9 T is distinctly smaller than the expected saturation magnetization (see discussion above and Fig. 2) as well as the "missing" entropy $S_{mag} < R \ln 17$. We note that also in the case of HoIr$_2$Si$_2$ a saturation value of $S_{mag} \sim R \ln 12$ was reported [57], suggesting a common origin for finding a reduced S_{mag} at high temperatures in both compounds.

Having both $\alpha_i(T)$ and $C_p(T)$ at hand, the Grüneisen ratio can be evaluated. For a single, dominating contribution to the entropy S with characteristic energy scale T_j, the Grüneisen ratio Γ_j is expected to be independent of temperature [58–60]. Experimentally, this can be verified by analyzing the ratio α_i/C_p [61]. In our case, we focus on the magnetic contributions to α_i and C_p. In order to estimate the phonon contribution to α_i we make use of this contribution to C_p as described above and scale it to $\alpha_i(T = 70 \text{ K})$. After subtraction, the resulting magnetic part $\alpha_{\text{mag}}^{110}$ is presented for the direction (110) in the inset of Fig. 4(b) along with C_{mag} [from Fig. 5(a)] within $20 \leqslant T \leqslant 38$ K for direct comparison. Clearly, the two quantities scale reasonably well, with $\alpha_{\text{mag}}^{110}/C_{\text{mag}} \sim 1.6 \times 10^{-8}$ mol J^{-1}. Similarly good agreement is found for the (100) direction, with $\alpha_{\text{mag}}^{100}/C_{\text{mag}} \sim 1.2 \times 10^{-8}$ mol J^{-1}, while for (001) the agreement is not quite as nice. All this may indicate a common magnetic origin of the transitions at T_N and T_2. The transition at T_1 appears to be separate because of the much larger values of $\alpha_{\text{mag}}^i(T_1)$ compared to $\alpha_{\text{mag}}^i(T_2)$, while the opposite holds for C_{mag}. Because of the extremely sharp peaks of C_p and α_i at T_2 we find the population (or depopulation) of CEF levels as the cause of this transition to be unlikely. Rather, we speculate that a change in the magnetic structure takes place at T_2. The above-described simple AFM structure with $\vec{k} = (0, 0, 1)$ was established for $T \leqslant 27 \pm 1$ K [17]. This leaves the possibility of a different magnetic structure within $T_2 \leqslant T \leqslant T_N$. In fact, Ho itself displays several magnetic structures, including a helical one [62]. An incommensurate magnetic structure for $T_2 \leqslant T \leqslant T_N$ was suggested in [34] without showing the data. In addition, a change from an incommensurate ordering vector just below T_N to a commensurate one at lower T was reported for HoMn$_2$O$_5$ [63] and HoSbTe [64]; a similar sequence was observed for HoNi$_2$B$_2$C [65]. Therefore, a change in the magnetic structure at T_2 is certainly possible but awaits confirmation, e.g., by neutron scattering.

Beyond that, one may consider the impact of the magnetoelastic coupling on the structure of HoRh$_2$Si$_2$. For instance, in some tetragonal rare-earth nickel borocarbides a magnetostriction-induced orthorhombic lattice distortion was observed [66–68]. Here, the lattice distortion (expressed as the relative difference of the orthorhombic lattice parameters a and b) was reported to be proportional to the squared ordered magnetic moment around T_N [67]. In the case of HoRh$_2$Si$_2$, one may then speculate that the increase of the ordered magnetic moment upon cooling through T_N may also, via magnetoelastic coupling, induce a structural phase transition at T_2. Indeed, detailed measurements of $C_p(T)$ according to the recipe outlined in Ref. [40] exhibit a very sharp peak at T_2 [Fig. 5(c)]. In addition, the measurement platform temperature T_P stopped close to T_2 due to the sample's latent heat [40] [inset to Fig. 5(c)]. Both observations clearly indicate a first-order transition taking place at T_2, supporting the aforementioned scenario. However, high-resolution structural investigations in this T range are called for to substantiate such a speculation [50].

B. DyRh$_2$Si$_2$

Figure 6 displays the dc susceptibilities χ of one of our DyRh$_2$Si$_2$ single crystals with magnetic fields of 25 Oe
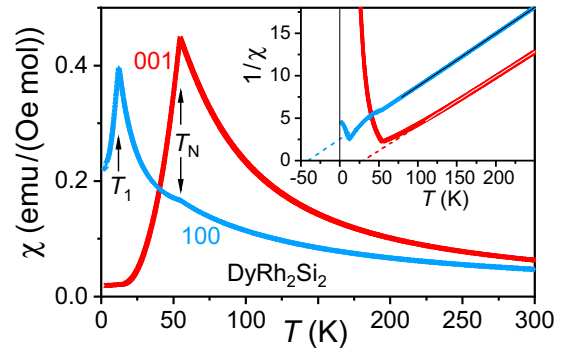
FIG. 6. dc susceptibility χ measured for DyRh$_2$Si$_2$ along the (100) and (001) crystallographic directions in fields of 25 Oe. Inset: inverse susceptibilities $1/\chi$ in units of Oe mol emu^{-1}. The dashed lines represent extrapolations of the linear fits (black and white lines) to $1/\chi$.

applied along the (100) and (001) directions. From this, $T_N = 54.7 \pm 0.5$ K and $T_1 = 12.0 \pm 0.2$ K were obtained. Fits of $1/\chi$ (see the inset in Fig. 6) yield effective moments of $\mu_{\text{eff}} \approx (11.2 \pm 0.5)\mu_B$ (the expected value for Dy^{3+} is $10.65\mu_B$). The deduced Weiss temperatures are $\theta_c \sim 30 \pm 0.8$ K along c and $\theta_a \sim -39 \pm 0.4$ K along the a direction, indicating qualitatively similar but somewhat larger interactions compared to HoRh$_2$Si$_2$. These values are consistent with the magnetic properties recently reported for DyRh$_2$Si$_2$ single crystals [33].

The magnetic behavior of DyRh$_2$Si$_2$ is qualitatively similar to that observed for HoRh$_2$Si$_2$ [see Figs. 1(b) and 6]. For both compounds, the magnetic moments align along the c direction below T_N [19,42] but tilt away from c for $T < T_1$. The larger Weiss temperatures of DyRh$_2$Si$_2$ are in line with its larger T_N compared to the Ho compound. Also, about two times larger magnetic fields (4.0 and 8.2 T [33]) are required for the steplike magnetization behavior in DyRh$_2$Si$_2$ with $\vec{H} \parallel (001)$, which is otherwise very similar to the one shown in Fig. 2. There is no indication for any other transition in DyRh$_2$Si$_2$; i.e., there appears to be no counterpart to T_2 seen in HoRh$_2$Si$_2$.

Single crystals DyRh$_2$Si$_2$ exhibit a preferred natural growth edge along the [110] crystallographic direction [36]. Therefore, a suitable sample for measurements of thermal expansion along the (100) direction needed to be searched for. Some results for two different runs are presented in Fig. 7(a). Between these runs (denoted as runs 1 and 2) the single crystal was mounted afresh inside our measurement cell. As can clearly be seen, the two runs yielded quantitatively different results, although the transitions were always observed at very similar temperatures (or magnetic fields) and agree well with the results from other measurements (see below). The same holds for additional runs as well as measurements along the (110) and (001) crystallographic directions (not shown here). This indicates that our measurements are genuine. As in the case of HoRh$_2$Si$_2$, we may speculate that domain effects play a role in these differences, but other influences cannot be ruled out at present. We therefore restrict ourselves to a discussion of the transition temperatures (and transition fields in the case of magnetostriction) in the following.

Included in Fig. 7 are examples of results for $\alpha(T, H)$ obtained at different applied magnetic fields, here, $\mu_0 H = 2$ and
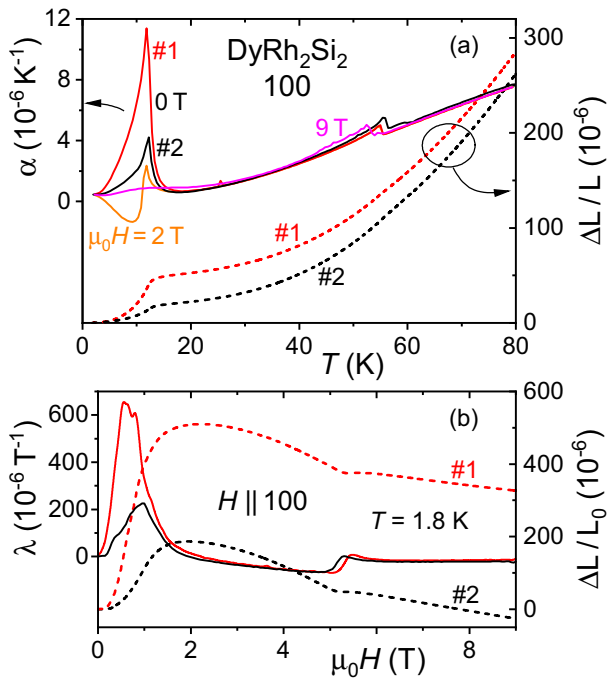
FIG. 7. (a) Two measurements of thermal expansion $\Delta L_{100}(T)/L_{100}$ (dashed lines, right scale) on a single crystal of $DyRh_2Si_2$, along with the thermal expansion coefficient $\alpha(T)$. Also included are examples of $\alpha(T, H)$ in applied magnetic fields for run 1. (b) Magnetostriction $\Delta L(H)/L_0$ at $T = 1.8$ K with magnetic fields applied along the (100) direction (dashed lines, up sweep). The magnetostriction coefficients λ (left scale) vary considerably in magnitude for $\mu_0 H \lesssim 1$ T.

FIG. 8. (a) Example of a thermal expansion measurement along (110). (b) Low-temperature–magnetic field (T–H) phase diagram of $DyRh_2Si_2$ with $\vec{H} \parallel$ (110). All blue data points, lines, and shading were taken from [33]. Our thermal expansion (stars) and magnetostriction (diamonds) results agree well with the reported data [33]. Green and red symbols indicate results from two different samples.

9 T. For the latter, T_N is reduced to ~ 53 K, while the transition at T_1 is largely suppressed to a faint, broad crossover. At such high in-plane fields, the magnetic moments rotate toward the field direction regardless of the presence or absence of any tilting away from the c direction due to the CEF.

An example of a thermal expansion measurement along the (110) direction is presented in Fig. 8(a) which is, not surprisingly, very similar to the (100) direction. The results of our measurements for $\vec{H} \parallel$ (110) are summarized in the low-temperature–magnetic field phase diagram in Fig. 8(b). All blue portions were taken from [33]. Obviously, the thermal expansion (red and green stars at zero field) and magnetostriction results agree nicely with these reported data. As mentioned earlier, results obtained for different samples (marked by red and green symbols) also agree well, and hence, the quantitative differences discussed above are not caused by sample dependences. Note that the temperature range of this phase diagram is well within the antiferromagnetic order, $T \ll T_N$. As mentioned, below $T_1 = 12$ K, the magnetic moments start to tilt away from the crystallographic c direction. Moreover, the (small) magnetocrystalline anisotropy within the basal plane gives rise to an additional feature in the phase diagram depending on whether the CEF-derived anisotropy or the applied magnetic field dominates energetically. As a result, one may expect a crossover, rather than a transition, which would explain the broad feature at $\mu_0 H < 1.5$ T observed in λ for $\vec{H} \parallel$ (110) [similar to the data shown in Fig. 7(b) for $\vec{H} \parallel$ (100)].

An example of magnetostriction measurements with $\vec{H} \parallel$ (001) at several temperatures is shown in Fig. 9(a). At $T = 60$ K, i.e., for $T > T_N$, only a very small and featureless field dependence of $\Delta L(H)/L_0$ is seen. As a result, we can safely assume that the steplike features observed in $L(H, T < T_N)/L_0$ are linked to the antiferromagnetic spin alignment. Plotting all the transitions observed in the magnetostriction measurements in a H-T phase diagram results in Fig. 9(b). Here, our data are overlayed onto the respective phase diagram in [33] (red data points, shading, and labels). The excellent agreement in Fig. 9(b) indicates that the two jumps observed in magnetostriction [Fig. 9(a)] are related to two consecutive spin-flip transitions from an antiferromagnetic $+ - + -$ state (marked AFM I) to $+ + + -$ (AFM II) beyond about 4 T and, finally, to a field-polarized (FP) $+ + + +$ state [33].

Our thermal expansion measurements [stars in Fig. 9(b)] conducted at different constant fields H reveal the presence of another transition which was not included in the earlier phase diagram [33]. As it is observed at $T \sim 12$ K, it is likely related to T_1, i.e., the temperature at which the magnetic moments tilt away from the crystallographic c direction. This tilting is a consequence of the strong anisotropy (i.e., large related CEF parameters [31–33]) along the c direction, and hence, it is not surprising to find this transition is nearly independent of H, even in the field-polarized state at $\mu_0 H = 9$ T [the maximum field of our PPMS; see the red curve in the inset of Fig. 9(a)]. The smaller (compared to the zero-field curve), but clearly visible, change in $\alpha(T, \mu_0 H = 9 \text{T})$ indicates that
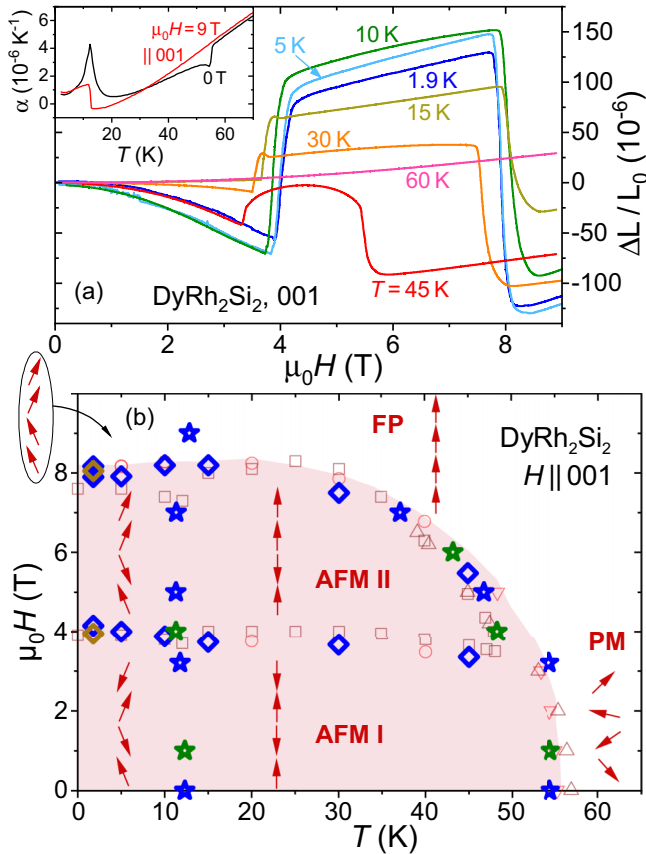
FIG. 9. (a) Exemplary magnetostriction $\Delta L(H,T)/L_0$ of DyRh$_2$Si$_2$ at several temperatures, $1.9 \leqslant T \leqslant 60$ K, with magnetic field applied $\vec{H}$ along the (001) direction. Inset: $\alpha(T, H)$ measured at 0 and 9 T for the same setup as in (a). (b) T-H phase diagram for $\vec{H} \parallel (110)$. All reddish data points, shading, and labels were taken from [33]. The results of thermal expansion and magnetostriction measurements are presented by stars and diamonds, respectively. Differently colored symbols (blue, green, dark yellow) mark results from different runs on two samples. The alignment of the magnetic moments is sketched by red arrows, along with a possible domain formation below T_1 (FP, field polarized; PM, paramagnetic).

right above ~8 T the magnetic moments are still not fully field aligned along (001) for $T < T_1$. Above T_1, the Dy moments appear to rotate smoothly in applied fields upon going from the paramagnetic state to the FP state, as suggested by the absence of any feature in $\alpha(T, \mu_0 H = 9 \,\mathrm{T})$. Interestingly, despite the almost two times higher T_N of DyRh$_2$Si$_2$ compared

to HoRh$_2$Si$_2$, the temperatures T_1 are nearly the same (12 and 11.7 K, respectively). Moreover, the tilting angle of ~25° at $T = 4.2$ K in DyRh$_2$Si$_2$ [19,31] is similar to the one in HoRh$_2$Si$_2$. The observation of a clear jump in $\alpha(T, \mu_0 H = 9 \,\mathrm{T})$ at $T_1 = 12$ K for $\vec{H} \parallel (001)$ but only a broad hump for $\vec{H} \parallel (100)$ [Fig. 7(a)] may again be related to the formation of magnetic domains [see sketch in Fig. 9(b)] but may possibly also be related to the (already mentioned) oblate shape of the $4f$ electron density [27].

IV. CONCLUSION

The compounds DyRh$_2$Si$_2$ and HoRh$_2$Si$_2$ share sizable effects in thermal expansion. In fact, they both exhibit a canting of the magnetic moments away from the crystallographic c direction upon cooling to temperatures below about 12 K which are reflected in positive peaks of $\alpha(T)$ for all main crystallographic directions. We attribute these similarities to similar CEF effects experienced by the rare-earth elements in both compounds as well as to similar $4f$ electron densities of the Dy^{3+} and Ho^{3+} ions. The latter may also serve as an explanation for the observed opposite changes in $\alpha(T)$ depending on whether it is measured parallel or perpendicular to the c direction of the tetragonal lattice [Figs. 4 and 7(a) and inset of Fig. 9(a)]. Unfortunately, a quantitative analysis beyond this qualitative comparison has proven difficult due to differences in the magnitudes of both α and λ for differently mounted samples, particularly in the case of DyRh$_2$Si$_2$. We attribute these differences to magnetic domain effects in these samples. This assumption is supported by the fact that in all measurements of $\alpha(T)$ and $\lambda(H)$ highly consistent transition temperatures or transition fields were observed, respectively.

One difference between the two compounds is the appearance of a second transition temperature T_2 close to, but distinct from, T_N in HoRh$_2$Si$_2$. This transition is seen in numerous properties: $\chi(T)$, $C_p(T)$, and $\alpha(T)$. Neutron diffraction measurements indicated a strong change in the intensity of the magnetic 100 reflection at 27 ± 1 K [17]. This observation may point to a change in the magnetic structure of HoRh$_2$Si$_2$ at T_2, an assessment in line with an analysis of the magnetic Grüneisen ratio.

[1] R. Hoffmann and C. Zheng, Making and breaking bonds in the solid state: The ThCr$_2$Si$_2$ structure, J. Phys. Chem. **89**, 4175 (1985).

[2] Q. Si, R. Yu, and E. Abrahams, High-temperature superconductivity in iron pnictides and chalcogenides, Nat. Rev. Mater. **1**, 16017 (2016).

[3] F. Steglich and S. Wirth, Foundations of heavy-fermion superconductivity: lattice Kondo effect and Mott physics, Rep. Prog. Phys. **79**, 084502 (2016).

[4] M. Shatruk, ThCr$_2$Si$_2$ structure type: The "perovskite" of intermetallics, J. Solid State Chem. **272**, 198 (2019).

[5] F. Steglich, J. Aarts, C. D. Bredl, W. Lieke, D. Meschede, W. Franz, and H. Schäfer, Superconductivity in the presence of strong Pauli paramagnetism: CeCu$_2$Si$_2$, Phys. Rev. Lett. **43**, 1892 (1979).

[6] T. T. M. Palstra, A. A. Menovsky, J. van den Berg, A. J. Dirkmaat, P. H. Kes, G. J. Nieuwenhuys, and J. A. Mydosh, Superconducting and magnetic transitions in the

heavy fermion system URu$_2$Si$_2$, Phys. Rev. Lett. **55**, 2727 (1985).

[7] R. Movshovich, T. Graf, D. Mandrus, J. D. Thompson, J. L. Smith, and Z. Fisk, Superconductivity in heavy-Fermion CeRh$_2$Si$_2$, Phys. Rev. B **53**, 8241 (1996).

[8] N. D. Mathur, F. M. Grosche, S. R. Julian, I. R. Walker, D. M. Freye, R. K. W. Haselwimmer, and G. G. Lonzarich, Magnetically mediated superconductivity in heavy fermion compounds, Nature (London) **394**, 39 (1998).

[9] E. Schuberth, M. Tippmann, L. Steinke, S. Lausberg, A. Steppke, M. Brando, C. Krellner, C. Geibel, R. Yu, Q. Si, and F. Steglich, Emergence of superconductivity in the canonical heavy-electron metal YbRh$_2$Si$_2$, Science **351**, 485 (2016).

[10] H. Q. Yuan, F. M. Grosche, M. Deppe, C. Geibel, G. Sparn, and F. Steglich, Observation of two distinct superconducting phases in CeCu$_2$Si$_2$, Science **302**, 2104 (2003).

[11] D. M. Broun, What lies beneath the dome? Nat. Phys. **4**, 170 (2008).

[12] B. Keimer, S. A. Kivelson, M. R. Norman, S. Uchida, and J. Zaanen, From quantum matter to high-temperature superconductivity in copper oxides, Nature (London) **518**, 179 (2015).

[13] Y. Lai, J. Y. Chan, and R. E. Baumbach, Electronic landscape of the f-electron intermetallics with the ThCr$_2$Si$_2$ structure, Sci. Adv. **8**, eabp8264 (2022).

[14] M. A. Ruderman and C. Kittel, Indirect exchange coupling of nuclear moments by conduction electrons, Phys. Rev. **96**, 99 (1954).

[15] T. Kasuya, A theory of metallic ferro- and antiferromagnetism on Zener's model, Prog. Theor. Phys. **16**, 45 (1956).

[16] K. Yosida, Magnetic properties of Cu-Mn alloys, Phys. Rev. **106**, 893 (1957).

[17] M. Ślaski, J. Leciejewicz, and A. Szytuła, Magnetic ordering in HoRu$_2$Si$_2$, HoRh$_2$Si$_2$, TbRh$_2$Si$_2$ and TbIr$_2$Si$_2$ by neutron diffraction, J. Magn. Magn. Mater. **39**, 268 (1983).

[18] I. Felner and I. Nowik, Itinerant and local magnetism, superconductivity and mixed valency phenomena in RM$_2$Si$_2$ (R = rare earth, M = Rh, Ru), J. Phys. Chem. Solids **45**, 419 (1984).

[19] M. Melamud, H. Pinto, I. Felner, and H. Shaked, Neutron diffraction study of the magnetic structure of the intermetallic compound DyRh$_2$Si$_2$, J. Appl. Phys. **55**, 2034 (1984).

[20] A. Szytuła, M. Ślaski, H. Ptasiewicz-Bąk, J. Leciejewicz, and A. Zygmunt, Magnetic ordering in NdRh$_2$Si$_2$ and ErRh$_2$Si$_2$, Solid State Commun. **52**, 395 (1984).

[21] M. Melamud, M. Kuznietz, H. Pinto, E. Caspi, and H. Shaked, Studies of magnetic interactions in some intermetallic AM$_2$X$_2$ compounds and their solid solutions, J. Magn. Soc. Jpn. **22**, S1_63 (1998).

[22] Z. Hossain, A. K. Rajarajan, V. K. Anand, C. Geibel, and S. M. Yusuf, Magnetic properties of PrRh$_2$Si$_2$: A neutron diffraction study, J. Magn. Magn. Mater. **321**, 213 (2009).

[23] K. Kliemt, M. Hofmann-Kliemt, K. Kummer, F. Yakhou-Harris, C. Krellner, and C. Geibel, GdRh$_2$Si$_2$: An exemplary tetragonal system for antiferromagnetic order with weak in-plane anisotropy, Phys. Rev. B **95**, 134403 (2017).

[24] J. Sichelschmidt, K. Kliemt, M. Hofmann-Kliemt, and C. Krellner, Weak magnetic anisotropy in GdRh$_2$Si$_2$ studied by magnetic resonance, Phys. Rev. B **97**, 214424 (2018).

[25] K. Kliemt, J. Banda, C. Geibel, M. Brando, and C. Krellner, Bulk properties of single crystals of the valence-unstable compound SmRh$_2$Si$_2$, Mater. Res. Express **6**, 126104 (2019).

[26] Y. W. Windsor, A. Ernst, K. Kummer, K. Kliemt, C. Schüßler-Langeheine, N. Pontius, U. Staub, E. V. Chulkov, C. Krellner, D. V. Vyalikh, and L. Rettig, Deterministic control of an antiferromagnetic spin arrangement using ultrafast optical excitation, Commun. Phys. **3**, 139 (2020).

[27] J. D. Rinehart and J. R. Long, Exploiting single-ion anisotropy in the design of f-element single-molecule magnets, Chem. Sci. **2**, 2078 (2011).

[28] B. Chevalier, J. Etourneau, J. E. Greedan, J. M. D. Coey, and A. Maarouf, Single-crystal magnetic susceptibility of TbRh$_2$Si$_2$: Determination of anisotropic exchange parameters, J. Less-Common Met. **111**, 171 (1985).

[29] G. Czjzek, V. Oestereich, H. Schmidt, K. Łątka, and K. Tomala, A study of compounds GdT$_2$Si$_2$ by Mössbauer spectroscopy and by bulk magnetization measurements, J. Magn. Magn. Mater. **79**, 42 (1989).

[30] Y. Takano, K. Ohhata, and K. Sekizawa, Thermodynamic and magnetic properties of HoRh$_2$Si$_2$: A comparison between experiments and calculations in a crystal field model, J. Magn. Magn. Mater. **66**, 187 (1987).

[31] K. Tomala, J. P. Sanchez, and R. Kmieć, Magnetic and crystal field properties of DyRh$_2$Si$_2$ and ErRh$_2$Si$_2$ from ^{161}Dy and ^{166}Er Mossbauer spectroscopy, J. Phys.: Condens. Matter **1**, 9231 (1989).

[32] Y. Takano, H. Takigami, K. Kanno, and K. Sekizawa, Specific heat and magnetization of DyRh$_{2-x}$Co$_x$Si$_2$, J. Magn. Magn. Mater. **104–107**, 1367 (1992).

[33] K. Kliemt, M. Ocker, S. Krebber, S. Schulz, D. V. Vyalikh, C. Krellner, and D. Y. Usachov, Moment canting and domain effects in antiferromagnetic DyRh$_2$Si$_2$, Phys. Rev. B **107**, 224424 (2023).

[34] T. Shigeoka, T. Fujiwara, K. Munakata, K. Matsubayashi, and Y. Uwatoko, Component-separated magnetic transition in HoRh$_2$Si$_2$ single crystal, J. Phys.: Conf. Ser. **273**, 012127 (2011).

[35] N. Sanada, R. Watanuki, K. Suzuki, M. Akatsu, and T. Sakakibara, Successive magnetic orderings of rectangular components caused by conservation of paraquadrupolar state in magnetically ordered phase in TbCoGa$_5$, J. Phys. Soc. Jpn. **78**, 073709 (2009).

[36] K. Kliemt, M. Peters, F. Feldmann, A. Kraiker, D.-M. Tran, S. Rongstock, J. Hellwig, S. Witt, M. Bolte, and C. Krellner, Crystal growth of materials with the ThCr$_2$Si$_2$ structure type, Cryst. Res. Technol. **55**, 1900116 (2020).

[37] R. Küchler, A. Wörl, P. Gegenwart, M. Berben, B. Bryant, and S. Wiedmann, The world's smallest capacitive dilatometer, for high-resolution thermal expansion and magnetostriction in high magnetic fields, Rev. Sci. Instrum. **88**, 083903 (2017).

[38] R. Küchler, R. Wawrzyńczak, H. Dawczak-Dębicki, J. Gooth, and S. Galeski, New applications for the world's smallest high-precision capacitance dilatometer and its stress-implementing counterpart, Rev. Sci. Instrum. **94**, 045108 (2023).

[39] Quantum design, https://www.qdusa.com.

[40] J. C. Lashley, M. F. Hundley, A. Migliori, J. L. Sarrao, P. G. Pagliuso, T. W. Darling, M. Jaime, J. C. Cooley, W. L. Hults, L. Morales, D. J. Thoma, J. L. Smith, J. Boerio-Goates, B. F. Woodfield, G. R. Stewart, R. A. Fisher, and N. E. Phillips, Critical examination of heat capacity measurements made on a quantum design physical property measurement system, Cryogenics **43**, 369 (2003).

[41] S. Mugiraneza and A. M. Hallas, Tutorial: a beginner's guide to interpreting magnetic susceptibility data with the Curie-Weiss law, Commun. Phys. **5**, 95 (2022).

[42] I. Felner and I. Nowik, Local and itinerant magnetism and superconductivity in R Rh$_2$Si$_2$ (R = rare earth), Solid State Commun. **47**, 831 (1983).

[43] T. Jaworska-Gołąb, L. Gondek, A. Szytuła, A. Zygmunt, B. Penc, J. Leciejewicz, S. Baran, and N. Stüsser, Neutron diffraction and magnetization studies of pseudoternary HoRh$_{2-x}$Pd$_x$Si$_2$ solid solution ($0 \leqslant x < 2$), J. Phys.: Condens. Matter **14**, 5315 (2002).

[44] T. Shigeoka, T. Fujiwara, K. Matsubayashi, and Y. Uwatoko, Magnetization processes and phase diagram of HoRh$_2$Si$_2$ single crystal having a component-separated magnetic transition, J. Phys.: Conf. Ser. **391**, 012063 (2012).

[45] D. Y. Usachov, A. V. Tarasov, D. Glazkova, M. Mende, S. Schulz, G. Poelchen, A. V. Fedorov, O. Y. Vilkov, K. A. Bokai, V. S. Stolyarov, K. Kliemt, C. Krellner, and D. V. Vyalikh, Insight into the temperature-dependent canting of $4f$ magnetic moments from $4f$ photoemission, J. Phys. Chem. Lett. **14**, 5537 (2023).

[46] A. Hubert and R. Schäfer, *Magnetic Domains* (Springer, Berlin, 1998).

[47] S.-W. Cheong, M. Fiebig, W. Wu, L. Chapon, and V. Kiryukhin, Seeing is believing: visualization of antiferromagnetic domains, npj Quantum Mater. **5**, 3 (2020).

[48] C. Huhnt, W. Schlabitz, A. Wurth, A. Mewis, and M. Reehuis, First-order phase transitions in EuCo$_2$P$_2$ and SrNi$_2$P$_2$, Phys. Rev. B **56**, 13796 (1997).

[49] J. Ferstl, New Yb-based systems: From an intermediate-valent to a magnetically ordered state, Ph.D. thesis, TU Dresden, Germany, 2007, https://cuvillier.de/uploads/preview/public_file/2139/9783867273756.pdf.

[50] K. Sekizawa, Y. Takano, H. Takigami, and Y. Takahashi, Low temperature specific heats and magnetic properties of LaRh$_2$Si$_2$ and HoRh$_2$Si$_2$, J. Less-Common Met. **127**, 99 (1987).

[51] S. Seiro, Y. Prots, K. Kummer, H. Rosner, R. Cardoso Gil, and C. Geibel, Charge, lattice and magnetism across the valence crossover in EuIr$_2$Si$_2$ single crystals, J. Phys.: Condens. Matter **31**, 305602 (2019).

[52] J. C. Lashley, R. Stevens, M. K. Crawford, J. Boerio-Goates, B. F. Woodfield, Y. Qiu, J. W. Lynn, P. A. Goddard, and R. A. Fisher, Specific heat and magnetic susceptibility of the spinels GeNi$_2$O$_4$ and GeCo$_2$O$_4$, Phys. Rev. B **78**, 104406 (2008).

[53] C. M. N. Kumar, Y. Xiao, H. S. Nair, J. Voigt, B. Schmitz, T. Chatterji, N. H. Jalarvo, and T. Brückel, Hyperfine and crystal field interactions in multiferroic HoCrO$_3$, J. Phys.: Condens. Matter **28**, 476001 (2016).

[54] O. Stockert, J.-U. Hoffmann, M. Mühlbauer, A. Senyshyn, M. M. Koza, A. A. Tsirlin, F. M. Wolf, S. Bachus, P. Gegenwart, R. Movshovich, S. Bobev, and V. Fritsch, Magnetic frustration in a metallic fcc lattice, Phys. Rev. Res. **2**, 013183 (2020).

[55] A. Tari, *The Specific Heat of Matter at Low Temperatures* (Imperial College Press, London, UK, 2003).

[56] U. Walter, Treating crystal field parameters in lower than cubic symmetries, J. Phys. Chem. Solids **45**, 401 (1984).

[57] K. Kliemt, M. Bolte, and C. Krellner, Crystal growth and magnetic characterization of HoIr$_2$Si$_2$ ($I4/mmm$), J. Phys.: Condens. Matter **30**, 385801 (2018).

[58] E. Grüneisen, Über die thermische Ausdehnung und die spezifische Wärme der Metalle, Ann. Phys. (Berlin, Ger.) **331**, 211 (1908).

[59] P. Gegenwart, Grüneisen parameter studies on heavy fermion quantum criticality, Rep. Prog. Phys. **79**, 114502 (2016).

[60] V. A. Drebushchak, Thermal expansion of solids: review on theories, J. Therm. Anal. Calorim. **142**, 1097 (2020).

[61] R. Klingeler, J. Geck, S. Arumugam, N. Tristan, P. Reutler, B. Büchner, L. Pinsard-Gaudart, and A. Revcolevschi, Pressure-induced melting of the orbital polaron lattice in La$_{1-x}$Sr$_x$MnO$_3$, Phys. Rev. B **73**, 214432 (2006).

[62] W. C. Koehler, J. W. Cable, M. K. Wilkinson, and E. O. Wollan, Magnetic structures of holmium. I. The virgin state, Phys. Rev. **151**, 414 (1966).

[63] G. R. Blake, L. C. Chapon, P. G. Radaelli, S. Park, N. Hur, S.-W. Cheong, and J. Rodríguez-Carvajal, Spin structure and magnetic frustration in multiferroic RMn$_2$O$_5$ (R = Tb, Ho, Dy), Phys. Rev. B **71**, 214402 (2005).

[64] I. Plokhikh, V. Pomjakushin, D. J. Gawryluk, O. Zaharko, and E. Pomjakushina, Competing magnetic phases in LnSbTe (Ln = Ho, Tb), Inorg. Chem. **61**, 11399 (2022).

[65] A. I. Goldman, C. Stassis, P. C. Canfield, J. Zarestky, P. Dervenagas, B. K. Cho, D. C. Johnston, and B. Sternlieb, Magnetic pair breaking in HoNi$_2$B$_2$C, Phys. Rev. B **50**, 9668 (1994).

[66] C. Detlefs, A. H. M. Z. Islam, T. Gu, A. I. Goldman, C. Stassis, P. C. Canfield, J. P. Hill, and T. Vogt, Magnetoelastic tetragonal-to-orthorhombic distortion in ErNi$_2$B$_2$C, Phys. Rev. B **56**, 7843 (1997).

[67] A. Kreyssig, A. Schneidewind, M. Loewenhaupt, C. Ritter, J. Freudenberger, G. Fuchs, and K.-H. Müller, Magnetoelastic effects in rare earth nickel borocarbides, in *Rare Earth Transition Metal Borocarbides (Nitrides): Superconducting, Magnetic and Normal State Properties*, edited by K.-H. Müller and V. Narozhnyi (Kluwer Academic, Dortrecht, The Netherlands, 2001), pp. 181–186.

[68] R. Toft-Petersen, T. B. S. Jensen, J. Jensen, M. von Zimmermann, S. Sloth, F. W. Isaksen, N. B. Christensen, Y. Chen, K. Siemensmeyer, H. Kawano-Furukawa, H. Takeya, A. B. Abrahamsen, and N. H. Andersen, Magnetoelastic phase diagram of TbNi$_2$B$_2$C, Phys. Rev. B **97**, 224417 (2018).